Effect of cyclic ageing on the early-stage clustering in Al–Zn–Mg(-Cu) alloys

Sohail Shah [a,*], Elisabeth Thronsen [b], Constantinos Hatzoglou [a], Sigurd Wenner [b,c],
Calin D. Marioara [c], Randi Holmestad [b], Bjørn Holmedal [a]

[a] Department of Materials Science and Engineering, Norwegian University of Science and Technology (NTNU), N-7491, Trondheim, Norway
[b] Department of Physics, Norwegian University of Science and Technology (NTNU), N-7491, Trondheim, Norway
[c] SINTEF Industry, N-7465, Trondheim, Norway

ARTICLE INFO

ABSTRACT

The cyclic application of mechanical stress to aluminum alloys at room temperature, referred to as cyclic ageing, continuously injects vacancies, enabling dynamic precipitation of a fine distribution of solute clusters. These are uniformly distributed throughout the bulk and are responsible for enhancing the mechanical properties to comparable values as T6 conditions obtained by conventional artificial aging. The atomic structure of the clusters in two Al–Zn–Mg (-Cu) alloys is studied using atomically resolved transmission electron microscopy, and their size, volume density and chemistry are investigated using atom probe tomography. It was found that cyclic ageing yields a high number density of solute clusters exhibiting structural similarities to the GPI zones commonly observed after low temperature ageing in such alloys. A subsequent 10-day natural ageing allows both cluster nucleation and further cluster growth, without altering their atomic structure. As compared to natural ageing, the strengthening caused by the solute clusters is accelerated during cyclic ageing, due to dynamic precipitation. The copper containing alloy also had higher amounts of Mg and Zn. Still, a slightly lower number density of smaller clusters with lower Zn/Mg ratio formed in this alloy, both after cyclic aging and after natural aging. The higher strength of this alloy is attributed to a higher strength contribution from each cluster.

1. Introduction

The Al–Zn–Mg (-Cu) alloys are widely used in the aerospace and automotive industry primarily due to their high strength to weight ratio and high corrosion resistance. Having good formability, these alloys allow for a wide range of processing routes such as extrusion, rolling and forging [1–3]. The main strengthening mechanism is precipitation hardening which involves a high temperature treatment above the solvus line of the system, such as a solution heat treatment (SHT, at >400 °C), followed by a rapid quench to room temperature and artificial aging (AA). During the high temperature treatment, the solute is dissolved into the host Al matrix and will, together with the high density of vacancies form a supersaturated solid solution (SSSS) after the rapid cooling. This condition has the maximum precipitation potential that will be utilized during the AA (usually at temperatures between 120 and 200 °C) to form a high density of nano-sized metastable precipitates, strengthening the material by providing obstacles for dislocation motion.

However, the SSSS is unstable even during natural ageing (NA) at room temperature, in which case the material gradually hardens due to formation of atomic clusters that are coherent with the aluminum lattice. When the clusters achieve periodic order in one or more spatial dimension, they are often referred to as Guinier-Preston (GP) zones [4, 5]. Two types of GP zones have been reported for the Al–Zn–Mg alloy system, namely the spherical GPI zones and the plate-like GPII zones [6].

The general precipitation sequence during artificial ageing is given as

$$SSSS \rightarrow atomic\ clusters \rightarrow GP\ zones \rightarrow \eta' \rightarrow \eta \qquad (1)$$

Recently, Sun et al. [7] have demonstrated a new approach for precipitating a very high number density of clusters, leading to strengths equal to and even higher than those from conventionally aged materials. The novel cyclic strengthening approach involves cyclic deformation of a solution heat treated and quenched material. During plastic deformation, the back-and-forth gliding of dislocations creates vacancies produced during dragging of jogs. These excess vacancies aid local diffusion. Some dislocation loops were present in the microstructure, but the extremely fine distribution of solute clusters being formed,

---

contributes to a major part of the strength, in a similar manner to that of the conventional artificially aged samples. Clusters observed in that study were suggested to not be the same type as those formed during conventional NA (the GPI and GPII zones).

Dynamic precipitation has been studied for a variety of heat-treatable aluminum alloys, and promising strength and work hardening have been reported [8–12], while other aspects like influence of the crystallographic texture, fatigue and fracture properties are still lacking. Studies focusing on the atomic structure of the clusters precipitated during cyclic strengthening, are sparse. In the present study, we aim at investigating the crystal structure of such clusters and compare them with the clusters precipitated during long-time storage, i. e., NA.

Recently, the atomic structure of the GPI zones in the 7xxx alloy system was determined [13]. The study showed that the GPI zones are built with a single building block that connects along certain directions in the Al matrix to form larger particles. The basic unit can be described as a truncated cube octahedron (TCO), consisting of three shells centered on a possible interstitial. The first shell consists of the atoms at the corners of the six faces of an inner octahedron and are occupied by Zn atoms. The second shell is an inscribed cube, for which the eight corners are occupied by Mg. The corner atoms of the octahedron are located at the cube centers. The last shell is a TCO. Its 24 vertices are ideally occupied by Zn, while the corners of the cube are located at the centers of the hexagonal faces of the TCO. The TCO can connect along $<001>$Al with its unique axis [001]GPI. Normal to its unique axis it can connect along $<411>$Al and $<330>$Al. Mixing of the $<411>$Al- and $<330>$Al connections is common, hence the individual GPI zones show variation in structure.

The focus of this study is to systematically compare the clusters formed in two commercial 7xxx alloys immediately after cyclic ageing. Their stability during NA is assessed and the effect of 10 days further storage at room temperature is characterized. Emphasis is placed on characterization of the structure and chemistry of these clusters in relation to the conventional GPI zones formed by NA.

2. Materials and methods

2.1. Materials

Two commercial alloys are studied, both received as extruded 6 mm thick plates from Benteler automotive. The compositions of the two alloys are given in Table 1. Both the alloys had similar texture. The major difference is that the 7046 contains copper and is slightly denser in solute than the 7003. The samples were SHT at 480 °C for half an hour in a salt bath followed by water quenching.

Peak Aged (PA) samples were also prepared for comparison with samples strengthened by cyclic deformation. Peak ageing heat treatment for these two alloys involved heating the samples up to 140 °C for 7 h (16.4 °C per hour) and keeping them at 140 °C for 17 h. The microstructure of PA samples is well known to consist of developed plate shaped η', along with $η_{1-2}$ [14,15]. Only the mechanical strengths were used for comparison. NAed samples from both alloys were also used to compare the structure of clusters formed during CA with the GPI zones formed during conventional NA. Long NAed samples with stabilized hardness were also used for comparison of strength contributions with the CA samples.

Table 1
Alloy composition of the investigated alloys (in wt.% and at.%).

		Cu	Fe	Mg	Si	Ti	Zn	Zr	Al
7046	wt%	0.28	0.2	1.31	0.08	0.03	6.47	0.15	Bal.
	at%	0.12	0.1	1.52	0.08	0.00	2.79	0.05	
7003	wt%	0.01	0.22	0.73	0.09	0.02	5.68	0.15	Bal.
	at%	0.00	0.11	0.84	0.09	0.01	2.43	0.05	

2.2. Cyclic ageing and hardness measurements

Samples for cyclic ageing (CA) tests, with the tensile axis along the extrusion direction, were machined. As shown in Fig. 1(a), they were flat-shaped with a square cross section of 6 mm thickness and width. The uniform length was 12 mm. CA tests, comprising of tension-compression following a sinusoidal waveform for the applied force, as seen in Fig. 1 (b), were carried out at a range of different frequencies. Initially, the stress amplitude was set around the yield strength (YS) of the SHT condition. The stress amplitude was gradually increased during the CA, up to a target stress. To ensure the CA samples were not subjected to excessive plastic deformation, the target stress was chosen slightly below the YS of the PA condition and the frequency was optimized. The CA experiments were designed based on the studies by Hutchinson et al. [10] and Sun et al. [7]. The stress amplitude was increased systematically, with the stress for cycle n given by:

$$\sigma_n = \sigma_0 + (\sigma_t - \sigma_0)\sqrt{\frac{n}{N}}. \tag{2}$$

Here σ_0 and σ_t are the initial and target stress amplitude strength. An optimization study had been carried out previously guiding how to optimally choose the target stress and the number of cycles N to reach it. The ideal condition for each alloy was applied, and the clusters in the resulting condition were studied by transmission electron microscopy (TEM) and atom probe tomography (APT). The optimization study will be published as part of a separate article.

Flat pieces from the tensile samples were ground and polished for micro-hardness measurements using a 1000 gf Vickers indenter. The mean hardness values were based on 5 readings each.
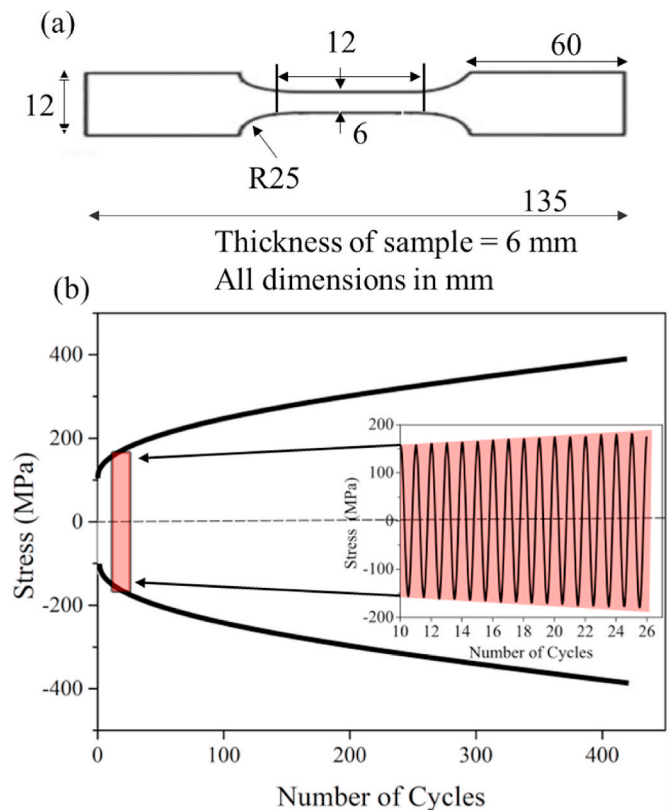

Fig. 1. (a) Geometry of test specimen used for cyclic ageing and tensile tests, (b) cyclic ageing profile. Insert shows a section of the gradual increase in stress amplitude.

2.3. APT sample preparation, acquisition parameters and cluster characterization methodologies

Electropolishing is preferred preparation methodology to avoid the contamination by ion implantation techniques. However, attempts to prepare the cyclic aged samples by electropolishing did not succeed. Hence, the APT needles from the cyclic aged material were prepared according to the conventional focused ion beam (FIB) lift out method [16] using the FEI Helios G2 dual beam instrument with a Ga^+ ion source. The needles were sharpened to around 50–100 nm using an 8 kV Ga^+ beam, followed by a 2 kV final clean-up step to remove higher concentrations of implanted high-energy Ga ions.

APT samples from the 3 months NA condition were prepared by following a standard two-step electropolishing process [17]. Rods of 0.3 $\times$ 0.3 $\times$ 20 cm^3 were cut from the samples and mechanically ground. The first step of the electropolishing was done using 25 vol% perchloric acid in 75 vol% acetic acid. The final step was a two-step process using 10 vol% perchloric acid followed by 2 vol% perchloric acid in 98 vol% 2-butoxylethanol to produce sharp needles. APT analysis was carried using a Local Electrode Atom Probe (LEAP) 5000XS by Cameca Instruments Inc. This is a straight flight path instrument with a detection efficiency of about 80%. All samples were run at 30 K base temperature in laser mode with a detection rate of 0.5%. An equivalent pulse fraction of 20% was used and calibrated in the range of 55–110 pJ, depending on the sample geometry. The pulse rate used was 250 kHz for all samples. Datasets, ranging from 50 to 150 million ions, were collected for the CA material. The reconstructions and the post processing analyses were carried out using the Integrated Visualization and Analysis Software (IVAS) by Cameca Instruments Inc. Complementary to IVAS, the Norwegian Atom Probe App (NAPA) software has been used. It has been developed by C. Hatzoglou from the Norwegian University of Science and Technology (NTNU) and is an open access software dedicated to APT data treatment [18]. The accurate estimation of the reconstruction parameters was carried out using the structural information and following the protocols of Gault et al. [19]. Sub-volumes were carefully chosen from APT datasets of cyclic aged samples for performing cluster analyses from regions without Ga implantation and away from the poles. The NA 3-month conditions were prepared by electropolishing and hence contained no Ga implantation, making the whole dataset suitable for analysis.

The "isoposition method" (IPM) was used to identify clusters in all the APT datasets. This method developed at the Groupe de Physique des Materiaux (University of Rouen, France) is based on chemical concentration (i.e., Mg + Zn) and atomic distance criteria. A detailed explanation of this algorithm and its criteria estimation can be found elsewhere [20,21]. The identified clusters exhibit an over atomic density compared to the matrix (up to 4–5 times higher), plus a morphological distortion (spherical in TEM, Fig. 5 and ellipsoidal in APT). This is due to the local magnification effect typically seen due to difference in evaporation fields between cluster/matrix during APT analysis [22,23]. The cluster dimension along the evaporation direction (i.e. Z direction) remains unchanged by local magnification as previously reported in Refs. [24,25]. The size of the clusters is so estimated from the Extent z (E_z) parameter, obtained from the cluster analysis. This parameter is defined as

$$E_z = |Z_{max} - Z_{min}| \tag{3}$$

where Z_{max} and Z_{min} are the outermost atoms of the cluster in the z-direction (the direction of evaporation). Considering local magnification effects, this is the least biased direction in the APT. E_z is based on the maximum distance between cluster atoms in this direction. The size and composition errors were calculated based on the standard deviation between the clusters while the error of the number density was calculated by dividing the number density by the square root of the total number of clusters. The clusters at the edge of the dataset which are not

completely inside are considered contributing half to estimate the number density.

Cluster finding algorithms have many drawbacks, because of parameter selection biasing [26], in particular for very small clusters with size ranging from 1 to 2 nm. An alternative method is used here, based on the pair correlation functions (PCF) obtained from the APT dataset, as illustrated in Fig. 3. It is a radial distribution function (RDF) based method with the advantage of being self-consistent, parameter free and uses the information from all atoms in the dataset. This methodology has previously been used to characterize precipitates in an Al–Cu-(Li–Mg) alloy system [27] as well as an Al–Zn–Mg system [28].

The approach makes use of an RDF calculated from the APT datasets, in which the specified species (in our case Zn and Mg) are examined. De Geuser et al. [29] introduced an γ_{i-j} pair correlation function between two elements by normalizing and scaling the RDF as

$$\gamma_{i-j}(r) = C_i C_{i-j}(r) - C_i C_j \tag{4}$$

where C_i and C_j are the bulk compositions of the respective elements obtained from the APT dataset, and $C_{i-j}(r)$ is the average composition of element j at a distance r. This is obtained from the atoms of element i obtained from the RDF.

For $i = j$, i.e., correlations of the same element, Eq (4) can be written as

$$\gamma_{i-i}(r) = C_i C_{i-i}(r) - C_i^2 \tag{5}$$

Also, when there is no correlation, which is the case for large r values, $\gamma_{i-i}(r) = 0$. At $r = 0$, the PCF corresponds to the mean square composition fluctuation, i.e. of precipitates and matrix, and can be written as,

$$\gamma_{i-i}(0) = \Delta C_i^2 = (C_p - C)(C - C_m) \tag{6}$$

where, C, C_m, and C_p are the bulk, matrix, and precipitate compositions respectively. The mean square compositional fluctuation (ΔC_i^2) is observed at $r = 0$ and decreases to zero as r increases with a characteristic correlation length which relates to the size of the compositional fluctuations (precipitates/clusters).

2.4. TEM sample preparation and acquisition parameters

For TEM specimen preparation, the samples were first mechanically thinned down to ~100 μm. The specimens were punched out to 3 mm disks and subsequently electropolished with a Struers TenuPol-5 machine using an electrolyte consisting of 1/3 HNO_3 and 2/3 CH_3OH. The electrolyte was kept at $-25\,°C \pm 5\,°C$ and the applied voltage was 20 V. An image- and probe corrected JEOL ARM200CF microscope, operated at 200 kV, was used for high-angle annular dark-field scanning TEM (HAADF-STEM) imaging. The convergence semi-angle was 27 mrad and the inner and outer collection semi-angles were 68 and 155 mrad, respectively. The probe current was about 60 pA, which gives a good signal, while maintaining sufficient spatial resolution. The images were filtered by performing a fast Fourier transform (FFT) and superimposing a low-pass mask on the FFT of approximately 6.7 nm^{-1}, before performing an inverse FFT.

3. Results

3.1. Hardness

The hardness immediately after quenching was recorded and the subsequent reading was taken directly after CA, which took 4 h and 40 min for the optimized condition running at 0.025 Hz. The results are shown in Fig. 2 for both alloys. The hardness of the grip region of the CA samples was also measured as a reference. Since this region did not undergo CA and is assumed unaffected, it gives a precise estimation of
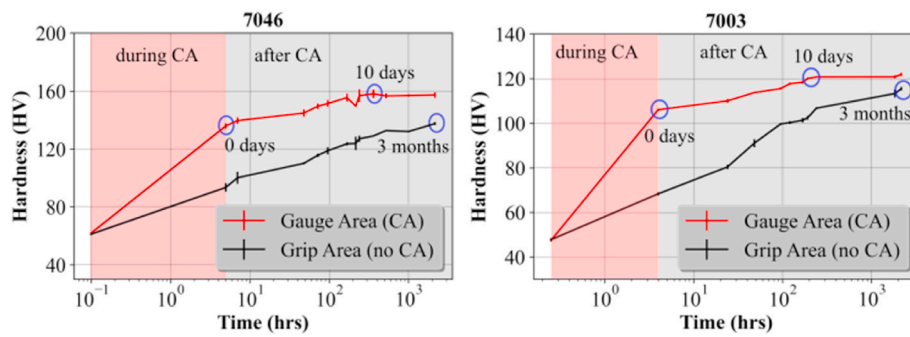
Fig. 2. Hardness evolution after SHT and quenching follows the red curves, highlighting the hardness evolution of the CA samples. The black curves show the corresponding NA evolution. The blue circles indicate the conditions studied by TEM and APT.
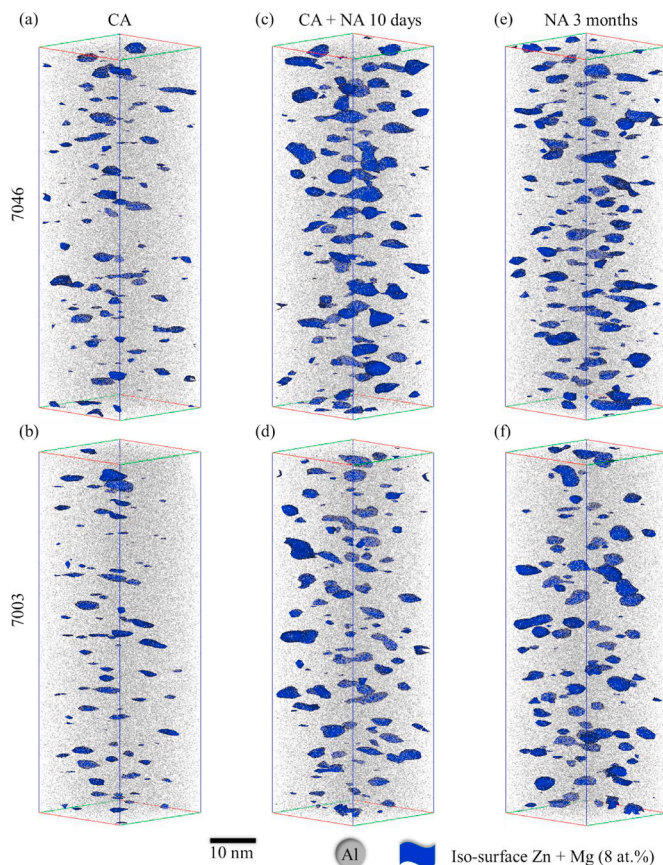

Fig. 3. Sub-volumes within the dataset of dimensions $25 \times 25 \times 80$ nm^3 to spatially visualize the clusters. The three conditions shown are (a) CA (c) CA aged + NA 10 days (e) NA 3 months for 7046 and (b) CA (d) CA + 10 days NA and (f) NA 3 months for 7003.

the hardness evolution by NA during the time spent performing the CA. Sample preparation for both TEM and APT took around 3 h for all conditions analyzed. As expected, the 7046 alloy was stronger than the 7003 alloy, due to its higher alloying content and Cu addition, c.f. Table 1 [30]. The hardness of 7046 was 61 ± 2 HV after solutionising and increased to around 135 ± 3 HV during the CA treatment. At the same time, the hardness at the grip area (NA) increased to 96 ± 3 HV. A similar trend was observed for 7003, where the hardness sharply increased from the as quenched (AQ) state at 47 ± 2 HV to 105 ± 1 HV after CA.

For both alloys, there was a gradual increase in hardness during NA after CA. After 10 days at room temperature, it almost saturated to a hardnesses of around 158 ± 2 HV and 121 ± 2 HV for 7046 and 7003, respectively. Selected samples were chosen for detailed APT and TEM analysis, as indicated with blue circles in Fig. 2.

3.2. APT data interpretation

APT analyses for all three conditions (CA, CA + NA 10 days and NA 3 months) show a high number density of fine solute clusters (of the order of 10^{24} clusters/m^3) for both alloys, see Fig. 3. As seen in Fig. 3(c) and (d), the 10 days of storage (NA) after the CA resulted in slightly larger clusters compared to the ones after CA, shown in Fig. 3(a) and (b) for 7046 and 7003, respectively. During this time the number density also increased, as seen from Table 2. Fig. 3(e) and (f) display the APT results of 3 months NA for 7046 and 7003, respectively, also showing a high number density of similarly sized spherical clusters. The size of the clusters in 7046 is consistently smaller compared to the ones in 7003 for the three conditions analyzed, but the difference in size is not large c.f. Table 2.

The chemistry of the clusters does not vary much between the three conditions of the same alloy, with an average Zn/Mg ratio of around 1.6 for 7046, and around 2.1 for 7003, see Table 2.

The clusters are rich in Mg and Zn and are in general spherical, which is evident from the cluster morphology maps shown in Fig. 4(a-c). Each map is divided into four quadrants, corresponding to disc, sphere, lath and rod. These are defined based on the oblateness and aspect ratio of

Table 2
Statistical results of cluster analysis for 7046 and 7003 alloys.

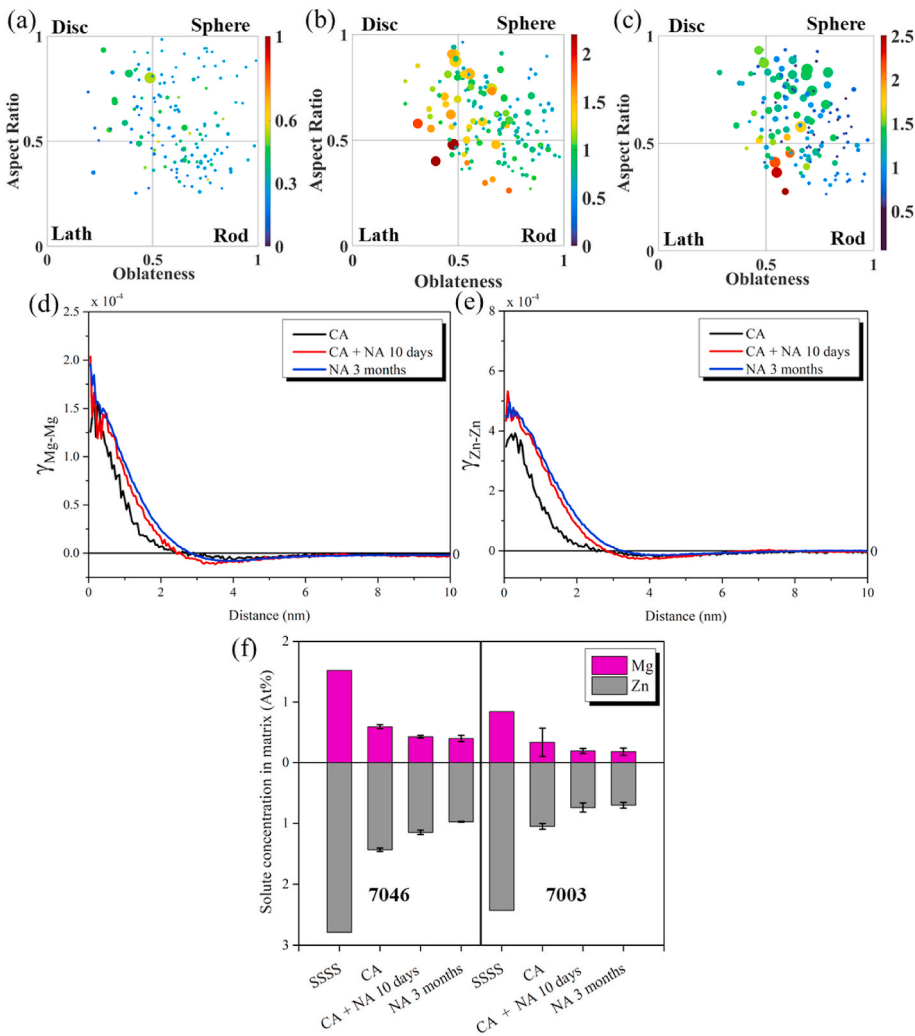| Alloy	Condition	Number Density (10^{24}/m^3)	Size (nm)	Zn/Mg	(Zn + Cu)/Mg
7046	CA	1.81 ± 0.19	1.12 ± 0.53	1.63 ± 0.49	1.66 ± 0.51
	CA + NA 10 days	3.15 ± 0.23	1.50 ± 0.89	1.58 ± 0.26	1.61 ± 0.27
	NA 3 months	2.11 ± 0.64	1.87 ± 0.65	1.53 ± 0.12	1.58 ± 0.11
7003	CA	3.75 ± 0.25	1.27 ± 0.44	2.14 ± 0.13	2.15 ± 0.14
	CA + NA 10 days	4.36 ± 0.27	1.57 ± 0.58	2.24 ± 0.25	2.21 ± 0.15
	NA 3 months	2.95 ± 0.67	2.01 ± 0.85	2.09 ± 0.14	2.10 ± 0.14

Fig. 4. Aspect ratio vs oblateness plots for clusters identified in the sub-volumes for CA, CA + NA 10 days and NA 3 months shown through (a–c) respectively for the 7003 alloy. The color scale shows the size of the clusters as radius of gyration in the evaporation direction while the size of the circles indicate the total number of atoms inside each cluster. Pair correlation functions for (d) Mg–Mg pairs and (e) Zn–Zn pairs from the APT datasets shown for 7003 in Fig. 3. The black line represents the theoretical PCF for a random distribution. (f) Zn and Mg concentrations in the matrix of the two alloys compared with the SSSS for different conditions.

the best fit of an ellipsoid to each cluster [31,32]. L_1, L_2 and L_3 are defined as the three major axes of each cluster, where $L_1 > L_2 > L_3$, and the aspect ratio (L_2/L_1) vs oblateness (L_3/L_2) is plotted in the cluster morphology map. Each circle represents one cluster and has a size proportional to the number of ions detected in that cluster.

Fig. 4(d) and (e) show the calculated Mg–Mg and Zn–Zn PCFs, respectively, for all datasets of 7003 shown in Fig. 3. Careful observation of the PCFs shows that the width of the PCF increases from CA to CA + NA 10 days and it is even larger at NA 3 months. As explained by De Geuser and Gault [33], an increased width of the PCF means an increased correlation length which in turn signifies the trend of increase in the size of clusters. This is the case for both Mg–Mg and Zn–Zn correlation lengths. The PCF for CA + NA 10 days and NA 3 months are almost identical and overlapping.

The solute concentration in the matrix in the clustered conditions was extracted based on the DIAM methodology from the APT datasets [34]. The results are summarized in Fig. 4(f). A high amount of solute in SSSS is consumed during the CA as the concentrations of Mg and Zn drop sharply from SSSS assuming all solutes dissolve during SHT. The solute consumption from the matrix continues after CA until the 10 days NA. Interestingly, 3 months NA has very similar solute content in the matrix as the CA + NA 10 days in both alloys.

Table 3 summarizes the contribution of SSSS to the yield strength estimated from the model of Deschamps et al. [35] as

$$\sigma_{sol} = K C_{sol}^{\frac{2}{3}} \tag{7}$$

where, σ_{sol} is the strength contribution from the solute in the matrix, $K = 840$ MPa is a constant adjusted to the yield strength of the material in SSSS and C_{sol} is the added volume concentrations of the solutes in the matrix; in our case sol corresponds to being Mg, Zn and Cu [36]. The K value for both alloys is chosen the same, since the effect of Cu is negligible due to very low concentrations of it in solid solution.

3.3. Atomic structure of the CA and NA clusters by TEM

Fig. 5 shows atomically resolved HAADF-STEM images of the microstructure in the three investigated conditions, CA, CA + NA 10 days and NA 3 months for the 7046 and 7003 alloys. All images are taken along the <001>Al zone axis. One overview HAADF-STEM image and two enlarged regions are shown for each condition. We could identify TCO structural units of the GPI zones [13] in all conditions of both alloys, and centers of TCOs are indicated with red disks in the enlarged regions, some of the disks are indicated by yellow arrows.

All three conditions exhibited a high number density of spherical clusters with varying sizes. Some clusters showed no clear atomic ordering, exemplified in Fig. 5a$_2$ and 5d$_2$ for 7046 and 7003, respectively. Such contrast might arise from clusters being far from the entrance surface or clusters consisting of randomly aggregated solutes rather than GP zones exhibiting clear atomic ordering. Most probably, a mixture of buried clusters and randomly aggregated solutes is present. The clusters that do exhibit ordering were all based on the same TCO structural units previously found in conventional NA samples [13,37].
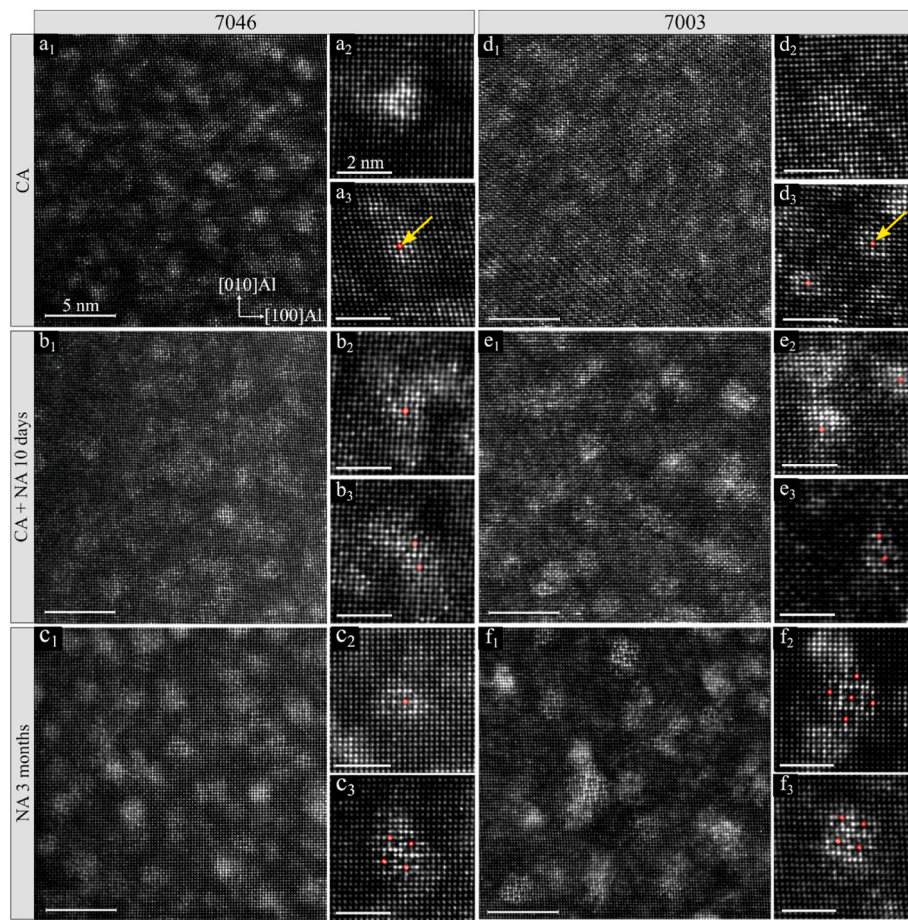
Fig. 5. Atomically resolved HAADF-STEM images along <001>Al for the three investigated conditions. a_1-f_1: Overview image for each condition. a_2-f_2 and a_3-f_3: Enlarged regions showing example clusters for each condition. The red disks along with the yellow arrows indicate the center of the TCOs. The lattice appears skewed in some images because of sample drift during image acquisition.

Table 3
Calculated contribution of SSSS to the yield stress based on APT measurements of solute levels in-between the clusters, and experimentally measured yield stress and UTS for the two alloys in the three investigated conditions. * indicates the yield stress and UTS from NA 1-year samples. This is done since the hardness measured has plateaued from 3 months to 1 year. The samples needed for tensile testing were not available in the 3 months NA condition.

Condition	YS from SSSS (MPa)		Experimental YS (MPa)		Experimental UTS (MPa)	
	7046	7003	7046	7003	7046	7003
CA	63.0	47.8	408	308	475	372
CA + NA 10 days	53.1	36.6	447	356	532	445
NA 3 months	48.5	35.3	368*	299*	534*	463*

Table 4
Quantification of the cluster microstructural differences in CA, CA + NA 10 days and NA 3 months based on the HAADF-STEM experiments. The clusters were categorized as single-, connected TCOs and disordered, and the numbers show their relative occurrence.

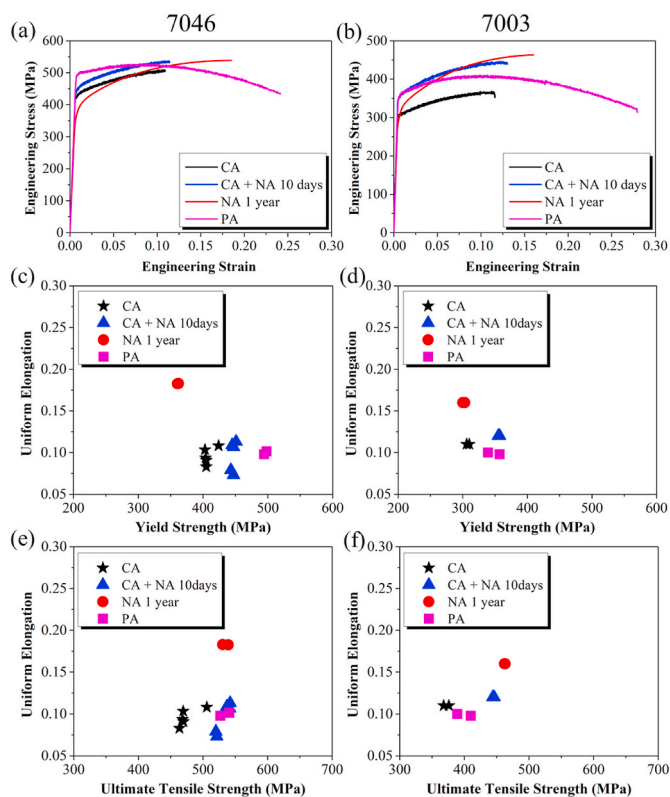| Alloy	Condition	Single TCO clusters	Connected TCO clusters	Disordered (no structure identified)
7046	CA	7%	0%	93%
	CA + NA 10 days	9%	1%	90%
	NA 3 months	8%	4%	88%
7003	CA	7%	0%	93%
	CA + NA 10 days	11%	2%	87%
	NA 3 months	4%	12%	84%

Fig. 6. Mechanical response of the two alloys subjected to CA, CA + NA, NA and artificial aging (PA). Engineering stress strain curves of (a) 7046 and (b) 7003. Correlation in YS and uniform elongation for (c) 7046 and (d) 7003. Correlation in UTS and uniform elongation for (e) 7046 and (f) 7003.

The main difference was that in CA conditions they always consisted of single TCOs, as highlighted in Fig. 5a₃ and 5d₃ by the red disks indicating the central atomic column of the TCO.

To investigate the microstructural evolution from CA to CA + 10 days NA and compare with the microstructure after NA 3 months, 300–400 clusters per condition were investigated. The clusters were investigated in terms of atomic ordering and categorized as single TCO, connected TCO and disordered. Their relative occurrence is shown in Table 4.

The microstructures after 10 days NA are shown in Fig. 5b₁ and Fig. 5e₁ for 7046 and 7003, respectively. Most of the ordered clusters were still single TCOs. A small population of connected TCOs were observed in this condition for both alloys. Such clusters are exemplified in Fig. 5b₃ and Fig. 5e₃ for alloys 7046 and 7003, respectively.

By comparing the appearance of the GPI zones in alloy 7046 with those in 7003 in the NA 3 months condition, there is a noticeable difference: alloy 7003 contains a higher fraction of clusters based on connected TCOs. This is exemplified in Fig. 5f₂ and f₃, where GPI zones consisting of 5 and 4 TCOs connected along the <411>Al directions are shown, respectively. In contrast, the GPI zones in 7046 more often consist of single TCOs, exemplified in Fig. 5c₂. This effectively implies that the clusters are in general coarser in alloy 7003 compared to those in 7046. About half of the connected GPI zones in the 3 months NA condition of alloy 7046 consist of multiple TCOs connected only along <411>Al, as exemplified in Fig. 5c₃.

3.4. Mechanical response

The engineering stress-strain curves from all the test conditions are shown in Fig. 6(a) and (b) for 7046 and 7003, respectively. Samples with NA for 1 year were used instead of NA 3 months to measure the effect of

long-term NA and compare it with the strength of the CA conditions.

Immediately after CA, the samples are consistently lower in YS than the artificially PA samples for both alloys but have higher uniform elongations. After further 10 days NA, the samples have higher YS and UTS than CA, but similar uniform elongation. For both alloys, the CA + NA 10 days condition results in higher UTS than the PA condition. For alloy 7003, the YS in the CA + NA 10 days condition is similar to, while for 7046 it is smaller than, the respective PA condition. The uniform elongation is significantly larger for the one-year NA condition, while for all other conditions is between 0.09 and 0.11 as summarized in Fig. 6 (c–f). For alloy 7003 the NA 1-year condition had YS similar to that immediately after the CA, while the YS of the CA condition of alloy 7046 was larger than the corresponding NA 1-year condition.

It is noted that the CA, as well as NA conditions, fractured very close to when they reached the maximum nominal stress. On the other hand, the PA condition for both alloys experienced a significant amount of necking before fracture occurred in the neck, as seen in Fig. 6 (a and b).

4. Discussion

The iso-position cluster analysis reveals a slight increase in size from CA to CA + NA 10 days and an even larger cluster size for the NA 3 months condition (c.f. Table 2). Note that due to local magnification effects and the resolution limit of the APT, it is challenging to quantify very small clusters with cluster identification algorithms [33]. The different composition and potential crystal structure of the particles compared to the matrix lead to differences in the electric field evaporation. The difference in evaporation field leads to a development of a local radius of curvature near the specimen surface and hence in the projection's image. This also causes trajectory aberrations and overlaps, not enabling the one-to-one mapping between the detector and the specimen surface. These errors will contribute similarly for the different samples, hence the relative differences should be more trustworthy than the precise size estimates.

As an alternative to the iso-position cluster analysis, the PCF approach can be used to assess the size estimate with good statistical significance. A comparison of the decay widths of the PCFs in Fig. 4 (d and e) indicates that the correlation lengths for both Mg–Mg and Zn–Zn pair correlations shows the same trend as the cluster sizes found by the iso-position method, and therefore gives the same conclusions. The PCF for the CA + NA 10 days and NA 3 months conditions are close, indicating that the sizes of the clusters are similar for these two conditions. Hence, it can be concluded that CA for a few hours induces accelerated kinetics, and after 10 days of storage, the cluster size is almost similar to NA for three months.

The strength increases about 50 MPa and 70 MPa for the 7046 and 7003 alloy respectively during the 10 days of storage after CA. During the same period of time, the concentrations of elements in solid solution, as estimated in Fig. 4(f), decays due to the consumption by the growing clusters. From Table 4, this contribution to loss of strength can be estimated to be about 10 MPa. Therefore, the measured strength increases must come from the evolution of clusters. As their number density has only a small increase while they grow (see Table 2), the increase in strength must therefore be caused by the larger clusters that act as stronger obstacles for the gliding dislocations.

The size of the clusters in the 7046 alloy is smaller, with slightly lower number densities estimated than in the 7003 alloy. However, the measured strength of 7046 is higher, as seen from Fig. 6 (a and b). To understand this, solute concentrations from the matrix was used to estimate the strength contribution from the atoms in solid solution. The solute concentration in the 7046 is higher than 7003 and contributes to increasing the strength of 7046 by about 15–20 MPa, according to the rough estimate by Eq. (7). However, as seen in Table 4, the difference in their strength from the experimental data is about 100 MPa, which cannot be adequately explained by the solute concentration difference. This suggests that a major part of the strength increase must stem from

differences in the intrinsic cluster characteristics. In other words, the Cu-containing clusters in alloy 7046 must be acting as stronger obstacles than the Cu-free clusters of similar size in alloy 7003. The other significant difference between the clusters in the two alloys is their average Zn/Mg ratio as seen in Table 2. The lower Zn/Mg ratio in the 7046 along with the presence of Cu must be the reason for the enhanced strengths of this alloy.

The HAADF-STEM images showed a large population of nano-sized clusters in both alloys after the CA treatment. As the specimen thickness in this work was around 30–40 nm, many of the clusters will be far from the electron entrance surface and such clusters will exhibit a lower contrast as compared to clusters close to the electron entrance surface. Due to this, the 'Disordered' category in Table 4 most likely also incorporates some TCO-based clusters.

The particles that did have a clear structure consisted of single TCOs, which is the basic building block of the GPI zones in Al–Zn–Mg (-Cu) alloys. A single TCO spans four (110)Al planes measured from corner to corner. This distance is $4d_{110} = 1.14$ nm. This fits well with the size of the clusters in the CA condition as measured by APT, which on the average was 1.1 nm and 1.3 nm for 7003 and 7046, respectively, c.f. Table 2.

Sun et al. postulated in their work that the clusters precipitated during CA should not be structurally similar to those observed during conventional natural aging, i.e. GP zones [7]. In our study however, we find that the CA clusters consisted of the same TCO building block that constructs the GPI zones in NA conditions. The main difference was that most of the structured CA clusters consisted of single TCOs, while the NA clusters consisted of aggregated TCOs. Consequently, the CA clusters must be smaller, which was proven in our work by the APT measurements c.f. Table 2. After CA + 10 days NA the microstructure consisted of more aggregated clusters, as compared to directly after the CA treatment. This aggregation was attributed to a combination of growth of the disordered clusters and the TCO clusters.

Earlier works on Al–Zn–Mg alloys have shown that the GPI zones nucleated after prolonged NA or in the early stages of AA most often consisted of connected TCOs rather than single TCOs [13,37]. In the present study this is only verified for the NA 3 months condition of the Cu-free 7003 alloy. For the Cu-containing 7046 however, more single TCOs compared to connected TCOs were observed in the NA condition. APT showed that the clusters in the 7046 alloy incorporated Cu for all three conditions. By investigating the Z-contrast in GPI zones in HAADF-STEM images we conclude that Cu most likely substitutes Zn in their structure, as this contrast is similar in both 7003 and 7046 alloys. If a significant amount of Cu substituted Mg, the Mg atomic columns of the GPI zones would have higher brightness in 7046 compared to 7003, which was not observed. A few atoms in the Zn atomic columns may be substituted with Mg without being observable with the TEM, but as we consistently observed that the Zn atomic columns were much brighter than the Mg atomic columns, this effect is expected to be minor.

A small-angle X-ray scattering (SAXS) investigation [38] has earlier shown that the addition of Cu decreases the nucleation radius of GPI zones. This is in accordance with our observations that 7046 has a smaller average cluster size than 7003 after CA and/or NA, supported both by APT and TEM. The addition of Cu is also known to refine the structure of η' [39], demonstrating that this effect is important for precipitates as well as clusters/GP zones. Upon comparing the CA clusters with the NA clusters for the Cu-free 7003, it is evident that the effect of CA is similar to that of Cu addition, reducing cluster size and increasing structural disorder.

It has been suggested [7] that the cyclic plastic deformation injects vacancies into the material from dragging of jogs on the gliding dislocations. This is assumed to increase the local substitutional diffusion kinetics, which enhance the precipitation and solute aggregation, and correspondingly strengthening the alloy. A 10-day NA after CA demonstrates a steady increase in the hardness, suggesting diffusion of elements in solid solution even after the CA.

The accumulated plastic strain during CA is large. By monotonic loading, e.g. cold rolling, this would give a significant strength contribution from dislocations being stored during deformation. However, during cyclic straining at low strain amplitudes, like during low-cycle fatigue, most of the storage of dislocations during tensile load are removed in the compression part of the cycle. Very few dislocations could be observed in the structure after CA, and the strength obtained was similar as by NA with a similar number density of GP-zones of comparable size. Hence, it can be concluded that the strength contribution from stored dislocations is small.

In both alloys, higher strengths are found in the 1-year NA and CA + NA 10 days conditions as compared to the strengths of the CA conditions without any NA. From Table 2 we see an increase in cluster density and size when subjecting the CA conditions to subsequent NA, which most likely is responsible for the strength increase. The 3 months NA conditions had lower cluster densities than the CA + NA 10 days, but the clusters were larger. The role of CA here is more of accelerated kinetics by pumping in vacancies and allow for nucleation of clusters with a higher number density. CA does not enhance the mechanical response compared to PA conditions for the alloys used in this study. It is known from the work by Hutchinson et al. [10] that the cluster number density keeps increasing during CA, while the cluster sizes remain more or less constant. They suggest that repeated shearing prevents further increase of the cluster sizes. The 10-day NA allows these clusters to slightly grow, which increases the area of the cross-sectional plane the dislocation must cut through and increases the surrounding misfit strain in the lattice. Hence, each cluster should be slightly more difficult to cut through by the gliding dislocations. This is important for achieving higher strength. This implies that the clusters immediately after CA still have the potential to grow during further NA at room temperature. As cluster density is smaller for the NA conditions, their larger clusters act as stronger obstacles to dislocation glide. The NA 1-year sample produced the highest tensile strength, as seen in Fig. 6(a and b).

Interestingly, and of importance for some applications, all samples for both alloys, with and without Cu, as processed with NA, CA, and also the samples with CA + 10 days NA, fractured abruptly during tensile testing. A slant ductile shear fracture was observed in all cases, without the commonly observed necking instability, i.e., without the diffuse necking expected for specimens with a square cross section. This is in contrast to the PA samples, which undergo significant amount of necking c.f. Fig. 6(a and b). Although the uniform elongations for the CA and NA samples are comparable with those of the PA conditions, fracture strains are severely compromised due to lack of post necking ductility. This is in contrast to what is earlier reported for CA [7]. An important difference is that earlier axisymmetric material and specimens are considered for a slightly different alloy. CA, although shows promise in the rapid hardening response, has constraints in specimen geometry in order to carry out tension and compression part of the test. However, there is potential for process innovation to carry out similar tests for commercial use. Tension and retraction to zero load can be possibly tried for large sheets where compression can be a challenge. Incremental bending and unbending can also be implemented to see the effect on the mechanical response.

5. Conclusion

Clusters nucleated during cyclic ageing and during natural ageing have been studied by APT and TEM for two Al–Zn–Mg (-Cu) alloys. One of the alloys contained Cu, while the other one was Cu-free. A high number of solute clusters were observed after cyclic ageing. After subsequent storage at room temperature cluster density and size increased, which correlated with increasing material strength. This saturated after 10 days of storage, suggesting that the clusters had stabilized. Storage at room temperature after CA is concluded to be very important for obtaining strength levels comparable to that of the peak age conditions obtained by artificial ageing.

When the same alloys were subjected to conventional natural aging for three months, slightly larger clusters were observed as compared to the CA conditions, but with similar chemistry. From TEM analysis of the atomic structure of the clusters it is concluded that the dynamically precipitated clusters are constructed with the same TCO structural unit as the GPI zones nucleated during conventional natural ageing. For both alloys, most of the structurally ordered clusters found in the CA and in CA + NA 10 days conditions consisted of single TCOs. Single TCOs were also found to dominate in the naturally aged Cu-containing 7046 alloy. The Cu-free 7003 alloy, on the other hand, contained a higher number density of connected TCOs along <411>Al and <330>Al in the naturally aged condition. The number density of clusters in the 7046 alloy, either natural or cyclic aged, was found to be similar or slightly lower, and the clusters smaller than in the 7003 alloy. The higher strength of natural or cyclic aged 7046 alloy could not be explained solely by a higher concentration of elements in solid solution. It is concluded that the Cu-containing clusters with a different Zn/Mg ratio to the 7003 alloy must be acting as stronger obstacles for dislocation glide, as compared to Cu free clusters of similar size.

Data availability

The raw data used to reproduce the presented results are available in the Zenodo repository http://doi.org/10.5281/zenodo.6344071.

CRediT authorship contribution statement

Sohail Shah: Supervision, conceived, designed, and supervised the research, conducted the CA experiments along with tensile testing, prepared the figures, Formal analysis, Writing – original draft, wrote the manuscript with input from all the authors. **Elisabeth Thronsen:** Supervision, Formal analysis, conceived, designed, and supervised the research, conducted the (S)TEM analysis, prepared the figures, Writing – original draft, wrote the manuscript with input from all the authors. **Constantinos Hatzoglou:** Formal analysis, conducted the APT measurements and analysis. **Sigurd Wenner:** Supervision, conceived, designed, and supervised the research, and. **Calin D. Marioara:** Supervision, conceived, designed, and supervised the research, and. **Randi Holmestad:** Supervision, conceived, designed, and supervised the research. **Bjørn Holmedal:** Supervision, conceived, designed, and supervised the research.

Declaration of competing interest

The authors declare that they have no known competing financial interests or personal relationships that could have appeared to influence the work reported in this paper.

Acknowledgement

References

[1] T. Dursun, C. Soutis, Recent developments in advanced aircraft aluminium alloys, Mater. Des. 56 (2014) 862–871, 1980-2015.

[2] O. Jensrud, High strength aluminium alloys extrusions-a review of the thermo-mechanical-process in high performance profile manufacturing, Key Eng. Mater. 491 (2012) 11–18. Trans Tech Publ.

[3] J. Hirsch, Recent development in aluminium for automotive applications, Trans. Nonferrous Metals Soc. China 24 (7) (2014) 1995–2002.

[4] A. Guinier, Structure of age-hardened aluminium-copper alloys, Nature 142 (3595) (1938) 569–570.

[5] G. Preston, The diffraction of X-rays by age-hardening aluminium copper alloys, Proc. Roy. Soc. Lond. Math. Phys. Sci. 167 (931) (1938) 526–538.

[6] V. Hansen, O. Karlsen, Y. Langsrud, J. Gjønnes, Precipitates, zones and transitions during aging of Al-Zn-Mg-Zr 7000 series alloy, Mater. Sci. Technol. 20 (2) (2004) 185–193.

[7] W. Sun, et al., Precipitation strengthening of aluminum alloys by room-temperature cyclic plasticity, Science 363 (6430) (2019) 972–975.

[8] W. Han, Y. Chen, A. Vinogradov, C. Hutchinson, Dynamic precipitation during cyclic deformation of an underaged Al–Cu alloy, Mater. Sci. Eng., A 528 (24) (2011) 7410–7416.

[9] A. Deschamps, G. Fribourg, Y. Brechet, J.L. Chemin, C. Hutchinson, In situ evaluation of dynamic precipitation during plastic straining of an Al–Zn–Mg–Cu alloy, Acta Mater. 60 (5) (2012) 1905–1916.

[10] C. Hutchinson, F. De Geuser, Y. Chen, A. Deschamps, Quantitative measurements of dynamic precipitation during fatigue of an Al–Zn–Mg–(Cu) alloy using small-angle X-ray scattering, Acta Mater. 74 (2014) 96–109.

[11] R. Pahl, J. Cohen, Effects of fatigue on the GP zones in Al-Zn alloys, Metall. Mater. Trans. 15 (8) (1984) 1519–1529.

[12] W. Han, A. Vinogradov, C. Hutchinson, On the reversibility of dislocation slip during cyclic deformation of Al alloys containing shear-resistant particles, Acta Mater. 59 (9) (2011) 3720–3736.

[13] A. Lervik, et al., Atomic structure of solute clusters in Al–Zn–Mg alloys, Acta Mater. 205 (2021), 116574.

[14] H. Löffler, I. Kovács, J. Lendvai, Decomposition processes in Al-Zn-Mg alloys, J. Mater. Sci. 18 (8) (1983) 2215–2240.

[15] A. Lervik, C.D. Marioara, M. Kadanik, J. Walmsley, B. Milkereit, R. Holmestad, Precipitation in an extruded AA7003 aluminium alloy: observations of 6xxx-type hardening phases, Mater. Des. 186 (2020), 108204.

[16] T.J. Prosa, D.J. Larson, Modern focused-ion-beam-based site-specific specimen preparation for atom probe tomography, Microsc. Microanal. 23 (2) (2017) 194–209.

[17] T.F. Kelly, M.K. Miller, Atom probe tomography, Rev. Sci. Instrum. 78 (3) (2007), 031101.

[18] Atom Probe Tomography (APT), Department of Materials Science and Engineering - NTNU.. https://www.ntnu.edu/ima/research/apt.

[19] B. Gault, et al., Advances in the calibration of atom probe tomographic reconstruction, J. Appl. Phys. 105 (3) (2009), 034913.

[20] J.M. Hyde, et al., Analysis of radiation damage in light water reactors: comparison of cluster analysis methods for the analysis of atom probe data, Microsc. Microanal. 23 (2) (2017) 366–375.

[21] W. Lefebvre, F. Vurpillot, X. Sauvage, Atom Probe Tomography: Put Theory into Practice, Academic Press, 2016.

[22] C. Hatzoglou, B. Radiguet, F. Vurpillot, P. Pareige, A chemical composition correction model for nanoclusters observed by APT-Application to ODS steel nanoparticles, J. Nucl. Mater. 505 (2018) 240–248.

[23] R. Lawitzki, P. Stender, G. Schmitz, Compensating local magnifications in atom probe tomography for accurate analysis of nano-sized precipitates, Microsc. Microanal. 27 (3) (2021) 499–510.

[24] F. Vurpillot, A. Bostel, D. Blavette, Trajectory overlaps and local magnification in three-dimensional atom probe, Appl. Phys. Lett. 76 (21) (2000) 3127–3129.

[25] F. Vurpillot, C. Oberdorfer, Modeling atom probe tomography: a review, Ultramicroscopy 159 (2015) 202–216.

[26] E.A. Marquis, J.M. Hyde, Applications of atom-probe tomography to the characterisation of solute behaviours, Mater. Sci. Eng. R Rep. 69 (4–5) (2010) 37–62.

[27] R. Ivanov, A. Deschamps, F. De Geuser, A combined characterization of clusters in naturally aged Al–Cu–(Li, Mg) alloys using small-angle neutron and X-ray scattering and atom probe tomography, J. Appl. Crystallogr. 50 (6) (2017) 1725–1734.

[28] H. Zhao, B. Gault, D. Ponge, D. Raabe, F. De Geuser, Parameter free quantitative analysis of atom probe data by correlation functions: application to the precipitation in Al-Zn-Mg-Cu, Scripta Mater. 154 (2018) 106–110.

[29] F. De Geuser, W. Lefebvre, D. Blavette, 3D atom probe study of solute atoms clustering during natural ageing and pre-ageing of an Al-Mg-Si alloy, Phil. Mag. Lett. 86 (2006) 227–234, 04.

[30] Y.-g. Liao, X.-q. Han, M.-x. Zeng, M. Jin, Influence of Cu on microstructure and tensile properties of 7XXX series aluminum alloy, Mater. Des. 66 (2015) 581–586.

[31] R.A. Karnesky, C.K. Sudbrack, D.N. Seidman, Best-fit ellipsoids of atom-probe tomographic data to study coalescence of γ′(L12) precipitates in Ni–Al–Cr, Scripta Mater. 57 (4) (2007) 353–356.

[32] R.K. Marceau, A. de Vaucorbeil, G. Sha, S.P. Ringer, W.J. Poole, Analysis of strengthening in AA6111 during the early stages of aging: atom probe tomography and yield stress modelling, Acta Mater. 61 (19) (2013) 7285–7303.

[33] F. De Geuser, B. Gault, Metrology of small particles and solute clusters by atom probe tomography, Acta Mater. 188 (2020) 406–415.

[34] F.D. Geuser, W. Lefebvre, Determination of matrix composition based on solute-solute nearest-neighbor distances in atom probe tomography, Microsc. Res. Tech. 74 (3) (2011) 257–263.

[35] A. Deschamps, Y. Brechet, Influence of predeformation and ageing of an Al–Zn–Mg alloy—II. Modeling of precipitation kinetics and yield stress, Acta Mater. 47 (1) (1998) 293–305.

[36] I. Zuiko, R. Kaibyshev, Deformation structures and strengthening mechanisms in an Al-Cu alloy subjected to extensive cold rolling, Mater. Sci. Eng., A 702 (2017) 53–64.

[37] E. Thronsen, et al., Studying GPI zones in Al-Zn-Mg alloys by 4D-STEM, Mater. Char. (2021), 111675.

[38] A. Deschamps, Y. Bréchet, F. Livet, Influence of copper addition on precipitation kinetics and hardening in Al–Zn–Mg alloy, Mater. Sci. Technol. 15 (9) (1999) 993–1000.

[39] K. Watanabe, K. Matsuda, S. Ikeno, T. Yoshida, S. Murakami, TEM Observation of precipitate structures in Al-Zn-Mg alloys with additions of Cu/Ag, Mater. Sci. Forum 794 (2014) 985–987. Trans Tech Publ.